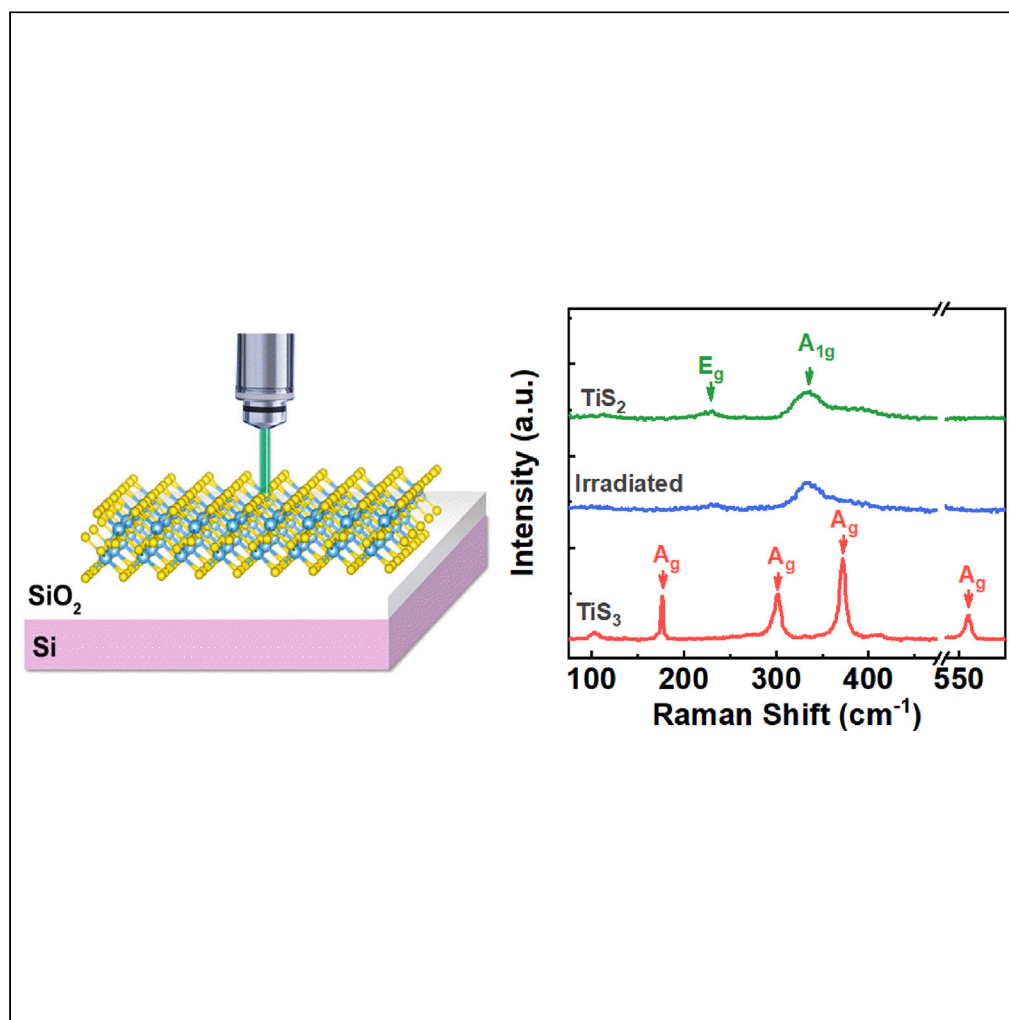**Article**

Laser irradiation induced structural transformation in layered transition metal trichalcogenide nanoflakes

Huifeng Zhang, Xiong Tu, Ziyu Wu, ..., Siyuan Wan, Ya-Qing Bie, Yangbo Zhou

bieyq@mail.sysu.edu.cn (Y.-Q.B.)
yangbozhou@ncu.edu.cn (Y.Z.)

Highlights

Local structural transformation from TiS_3 to TiS_2 using focused laser irradiations

Verification of heat-induced material decomposition mechanism of the transformation

Demonstration of in-plane TiS_3-TiS_2 heterostructures

Article

Laser irradiation induced structural transformation in layered transition metal trichalcogenide nanoflakes

Huifeng Zhang,[1,2,4] Xiong Tu,[1,2,4] Ziyu Wu,[1,2] Junqing Guo,[1,2] Linfeng Fei,[1,2] Xiaxia Liao,[1,2] Jiaren Yuan,[1,2] Siyuan Wan,[1,2] Ya-Qing Bie,[3,*] and Yangbo Zhou[1,2,5,*]

SUMMARY

Laser irradiation is a powerful tool in inducing changes in lattice structures and properties of two-dimensional (2D) materials through processes such as heating, bleaching, catalysis, etc. However, the underlying mechanisms of such transformations vary dramatically in different 2D materials. Here, we report the structural transformation of layered titanium trisulfide (TiS_3) to titanium disulfide (TiS_2) after irradiation. We systematically characterized the dependence of the transformation on laser power, flake thickness, irradiation time, and vacuum conditions using microscopic and spectroscopic methods. The underlying mechanism is confirmed as the heat-induced materials decomposition, a process that also occurs in many other transition metal trichalcogenide materials. Furthermore, we demonstrate that this spatial-resolved method also enables the creation of in-plane TiS_3-TiS_2 heterostructures. Our study identifies a new family of 2D materials that undergo a structural transformation after laser irradiation and enriches the methods available for developing new prototypes of low-dimensional devices in the future.

INTRODUCTION

Structural transformation in van der Waals materials have been widely observed as the atomic thin layers can be influenced and modified through the interactions with energetic particles[1–5] such as photons, electrons, and ions. The instability can be initiated via different mechanisms using these trigger methods. One useful way to modify the lattices with sub-micrometer spatial resolution in ultrafast timings is through optical irradiation. Typically, the laser spots with intense energy densities can raise the temperatures of the material at the focus, leading to a change of physical or chemical properties.[1] This change can occur through processes such as oxidation, sublimation, lattice degradation,[6–9] and phase transitions.[10–12] While some studies have been conducted on the structural transformation of graphene and transition metal dichalcogenides (TMDs), how to identify these transitions in other van der Waals materials and the underlying mechanisms remains a question.

As a typical van der Waals family member, the group-IVB transition metal trichalcogenides (MX$_3$, M: Ti, Zr, Hf; X: S, Se, Te) crystals are needle- or ribbon-like shapes, exhibiting unique physical properties such as metal-insulator transition,[13] tunable charge density wave,[14,15] anisotropic spectroscopic feature,[16,17] large birefringence, and linear dichroism responses.[18,19] Among them, the semiconducting titanium trisulfide (TiS_3) exhibits a direct band gap size of 1 eV, similar to that of silicon,[20] at its few-layer to monolayer limit,[21,22] making it particularly attractive for research into the next generation electronic and optoelectronic devices,[23,24] such as morphology-tailored transistors and broadband response photodetectors.[25–30] Thus, the thermal stability of MX$_3$ crystals is a critical issue for future applications. Previous studies have shown that they can be converted to transition metal dichalcogenides (MX$_2$) through a pyrolysis effect in a vacuum at high temperatures.[31,32] However, heating in ambient conditions results in a thermally activated oxidation process.[33,34] Although the laser-induced damages and oxidations on MX$_3$ flakes during spectroscopic characterizations[35,36] have been noticed and detailed, a systematic investigation is still needed to understand the structural transformation of MX$_3$ crystals under laser irradiations.

Here, we find that the monoclinic TiS_3 can be converted to the trigonal titanium disulfide (TiS_2) by irradiating it with a continuous-wave laser beam in a vacuum. The obtained 1T-TiS_2 flakes have been characterized using microscopic, spectroscopic, and electrical methods, and we attribute the mechanism behind structural transformation to the local heating of TiS_3 by the laser beam, causing the escape of one sulfur atom per unit cell. The transformation threshold power depends on the flake thickness, which is influenced by both the absorption in the layered

[1]Department of Materials Science, School of Physics and Materials Science, Nanchang University, Nanchang, Jiangxi 330031, P.R. China
[2]Jiangxi Key Laboratory for Two-Dimensional Materials, Nanchang University, Nanchang, Jiangxi 330031, P.R. China
[3]State Key Lab of Optoelectronic Materials and Technologies, Guangdong Province Key Laboratory of Display Material and Technology, Sun Yat-sen University, Guangzhou 510275, P.R. China
[4]These authors contributed equally
[5]Lead contact
*Correspondence: bieyq@mail.sysu.edu.cn (Y.-Q.B.), yangbozhou@ncu.edu.cn (Y.Z.)
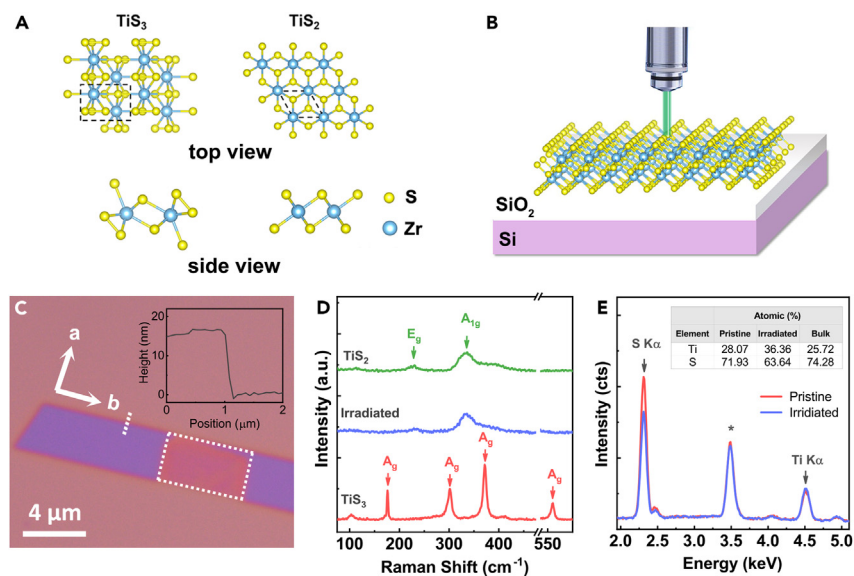https://doi.org/10.1016/j.isci.2023.107895

Figure 1. Structural transformation in TiS₃ induced by laser irradiation

(A) The top and side views of the crystal structures of monoclinic TiS₃ and trigonal TiS₂, respectively.

(B) Illustration of the laser irradiation on a TiS₃ flake on a SiO₂/Si substrate.

(C) An optical image of a ribbon-like TiS₃ flake. The height profile characterized by AFM in the inset figure shows that the flake thickness is 16 nm. The laser-irradiated region is outlined by a dashed rectangle.

(D) Raman spectra collected from the unirradiated and irradiated regions of the corresponding TiS₃ flake and a pristine TiS₂ crystal, respectively.

(E) EDS spectra collected from the pristine and irradiated regions of a TiS₃ flake. The S $K\alpha$ and Ti $K\alpha$ lines are indicated by the arrows, and the peak at 3.5 keV marked by the asterisk is the sum peak of Si $K\alpha$ lines. The inserted table shows the extracted atomic stoichiometric ratio from two regions, as compared to the value from a TiS₃ single crystal.

materials and the heat dissipation through the flake and the substrate. The focused laser beam is scanned to convert part of the TiS₃ flake into TiS₂, creating an in-plane heterostructure with different the electrical properties. Moreover, we applied that this laser-irradiation process to ZrS₃, ZrSe₃, and NbSe₃ which also underwent through a similar structural transformation. Our work thus has uncovered the transformation mechanism of the MX₃ materials and expanded the application of the laser processing technology for building low-dimensional electronic and optoelectronic devices in the future.

RESULTS AND DISCUSSION

The TiS₃ crystal, which belongs to the P2₁/m space group, has lattice constants of a = 4.973 Å, b = 3.433 Å, and c = 8.714 Å, respectively.[27] As shown in the left part of Figure 1A, each titanium atom is surrounded by six sulfur atoms, forming bicapped tetrahedrons that extend along the crystallographic b-axis. The formation of such quasi-1D chains in the crystal results in the anisotropic geometries and properties of TiS₃. Figure 1C shows an optical image of a mechanically exfoliated TiS₃ flake, which has a ribbon-like shape with a large aspect ratio. The flake exhibits purple color under white light illumination, corresponding to a thickness of approximately 16 nm (17 layers), as confirmed by atomic force microscopy (AFM) characterization (inset of Figure 1C). The Raman spectrum of TiS₃ is shown in Figure 1D as the red curve, which displays four peaks located at 172 cm⁻¹, 295 cm⁻¹, 363 cm⁻¹, and 554 cm⁻¹ within the collected spectral range. They are all identified as A_g modes of the monoclinic TiS₃ crystal as reported.[37,38] Since the intensities of these Raman modes are polarization dependent, we always set the laser polarization angle in parallel to the long edge of the ribbon during measurements to obtain the strongest Raman intensities.[17,35]

To investigate the effects of laser irradiations, a focused laser beam with a wavelength of 532 nm is applied to specific regions of the TiS₃ flake, as shown in Figure 1B. The irradiation conditions can be precisely controlled by adjusting the laser power, step size, and dwelling time during the scanning process. For example, the flake presented in Figure 1C was locally irradiated in a 5 × 3 μm² region using the raster scan mode with a step size of 100 nm and a dwell time of 0.1 s. The laser power was maintained at a constant 20 mW. The irradiation caused the flake color to change from blue to red in the irradiated region. The Raman spectrum collected from the irradiated region (blue curve in Figure 1D) shows the disappearance of all A_g modes of TiS₃, with two new peaks, emerging at ∼ 220 cm⁻¹ and 330 cm⁻¹, respectively. These changes indicate the destruction of the TiS₃ lattice and the formation of a new structure. The new structure could be correlated with trigonal TiS₂, whose crystal structure is presented in the right part of Figure 1A. This Raman spectrum exhibits peak profiles similar to that acquired from the high-quality TiS₂ crystal (green curve in Figure 1D, as we discover that it is difficult to exfoliate TiS₂ thin flakes, thus we use TiS₂ crystal instead, which would give similar results), with the two peaks identified as the E_g and A_{1g} modes of 1T-TiS₂, respectively.
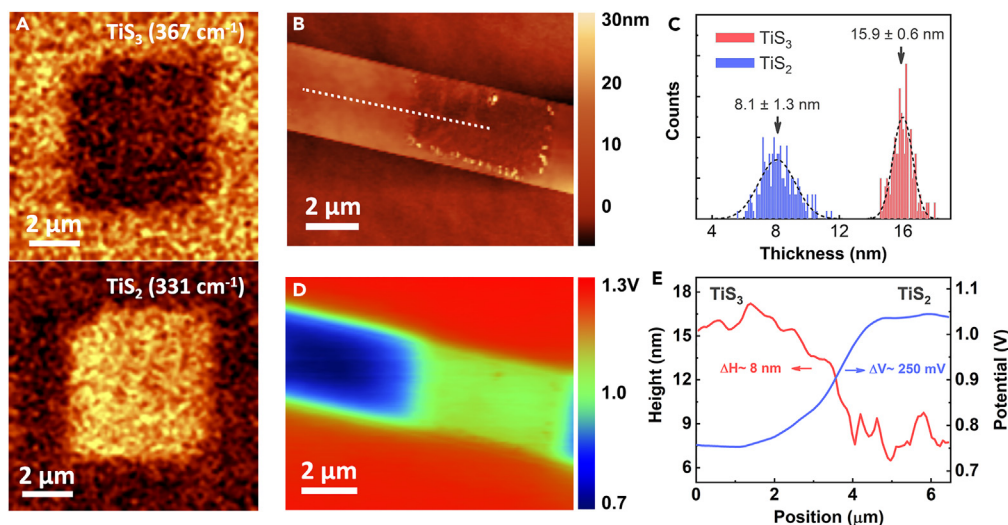
Figure 2. Morphology characterizations of laser-irradiated area

(A) Raman intensity maps using the A_g mode of TiS$_3$ centered at ~ 367 cm^{-1} (top view) and the A_{1g} mode of TiS$_2$ centered at ~ 331 cm^{-1} (bottom view), respectively.

(B) The AFM height image of the irradiated TiS$_3$ flake shown in Figure 1B.

(C) Histograms of thickness distributions collected from the unirradiated (TiS$_3$) and irradiated (TiS$_2$) regions.

(D) The KPFM image of the region as shown in (B).

(E) Variation of flake thickness (red line, corresponding to the left axis) and surface potential (blue line, corresponding to the right axis) across the irradiated flake along the dashed line in (B).

We then use energy-dispersive X-ray spectroscopy (EDS) to measure changes in the element stoichiometric ratio induced by laser irradiation. Figure 1E shows a comparison of the spectra collected from the unirradiated and irradiated regions of a thin flake on a SiO$_2$/Si substrate. In both spectra, several strong peaks can be observed in the analyzed spectral range, including the peaks of Ti $K\alpha$ (4.51 keV) and S $K\alpha$ (2.31 keV) lines. The additional peak located at 3.48 keV marked with an asterisk is attributed to the sum peak of the Si $K\alpha$ line (1.74 keV) that originates from the underlying SiO$_2$/Si substrate, which is an EDS spectral artifact.[39] The Si $K\alpha$ line is presented in Figure S1 as additional information. The intensity of the S $K\alpha$ line significantly decreases while the intensity of the Ti $K\alpha$ line maintains almost a constant, indicating the loss of sulfur element after laser irradiation. The quantitative analysis of the spectra gives a stoichiometric ratio of Ti:S = 28.07%:71.93% (1:2.56) for the pristine unirradiated flake, which deviates from the value of a TiS$_3$ crystal (25.72%:74.28%), as listed in the table shown in the figure. Such deviation may be attributed to the large signal errors in thin flakes. On the contrary, the irradiated region gives a stoichiometric ratio of 36.36%: 63.64%, close to that of a TiS$_2$ crystal. Therefore, by combining Raman and EDS analysis, we can deduce that laser irradiation results in a structural transformation from monocline TiS$_3$ to trigonal TiS$_2$.

We also discovered that the structural transformation process occurs uniformly in the laser-scanned regions. Figure 2A presents two Raman intensity maps collected from a 20 nm thick flake, with a laser-scanned region of 5 × 5 μm^2. These two maps are formed using the Raman peaks at 367 cm^{-1} (top view) and 331 cm^{-1} (bottom view), which corresponds to the A$_g$ mode of TiS$_3$ and A$_{1g}$ mode of TiS$_2$, respectively. The Raman modes of TiS$_3$ disappear in the irradiated region while exhibiting uniform intensity distributions in the unirradiated region; Conversely, the Raman modes of TiS$_2$ can only be observed in the irradiated region with uniform intensities. These Raman intensity distributions indicate that the original TiS$_3$ is uniformly transformed to TiS$_2$ during laser scanning, which is consistent with the uniform optical contrast in the converted region shown in Figure 1C. The treated flake in Figure 1C is characterized by the AFM height map as shown in Figure 2B, where the scanned region can also be clearly identified. The thickness histograms from both the irradiated and unirradiated regions show an increase in surface roughness from 0.6 nm to 1.3 nm, as indicated in Figure 2C. Meanwhile, the laser irradiation causes the reduction of flake thickness from 16 nm to approximately 8 nm, as presented by the height line profile across the irradiated region in Figure 2E. The laser-induced thinning effect is also observed in several TMD systems (MoS$_2$, MoTe$_2$, etc.).[1,6,10] In addition, we investigated the distribution of surface potential on this flake using Kelvin probe force microscopy (KPFM), with the corresponding KPFM map shown in Figure 2D. The irradiated region different colors (green) compared to the pristine TiS$_3$ (blue), indicating a higher surface potential and a lower work function caused by structural transformation. The potential difference is estimated to be $\sim$250 mV, as extracted from the corresponding potential line profile in Figure 2E. The difference is consistent with previous reports on the work function measurement for these two materials, where the defective TiS$_{2-x}$ exhibits a lower work function with a value difference of approximately 150 meV compared to TiS$_3$.[32,40]

To understand the mechanism underlying the structural transformation, we conducted a systematic study using Raman spectroscopy. We used single-spot irradiation instead of raster scanning since we did not observe significant differences. Figure 3A shows the Raman spectra collected from a 28 nm thick flake with increased laser powers. At a laser power of 7 mW, the Raman spectrum corresponds to
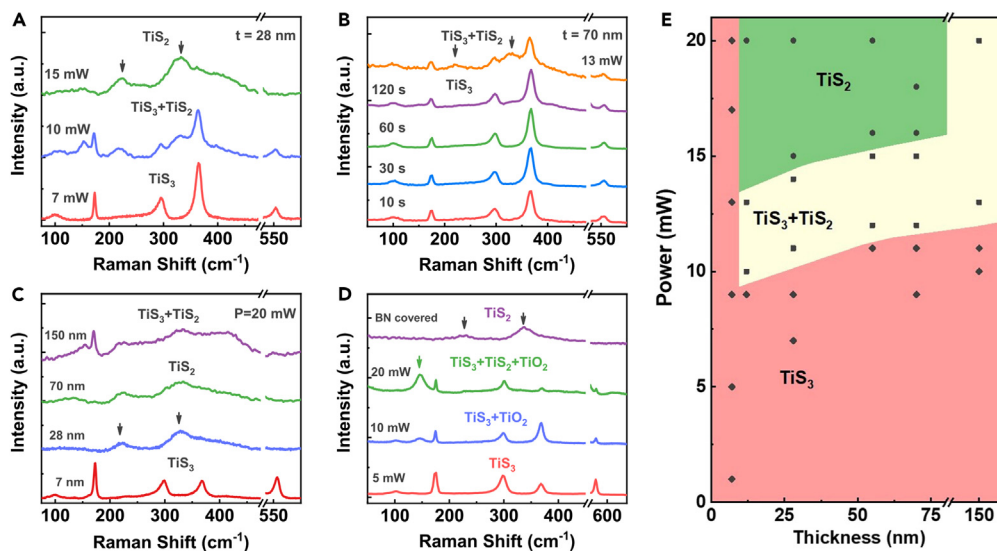
Figure 3. Controllability of the structural transformation

(A) Raman spectra of a 28 nm thick TiS_3 flake irradiated with different laser power in vacuum. The black arrows indicate the Raman modes of TiS_2. All the spectra shown here were using single spot acquisition mode instead of raster scanning.

(B) Raman spectra of a 70 nm thick TiS_3 flake with an excitation laser power of 12 mW and for durations ranging from 10 s to 120 s, and the spectrum excited at a higher power of 13 mW and for a duration of 10 s.

(C) Raman spectra of TiS_3 flakes with different thickness excited at a laser power of 20 mW.

(D) Raman spectra of a 35 nm thick TiS_3 flake irradiated with different laser powers in air. The purple line shows the spectrum of a transformed TiS_2 from a BN covered TiS_3 excited at a power of 20 mW. The additional green arrow indicates the appearance of TiO_2 peak.

(E) The structure transformation diagram as a function of flake thickness and laser irradiation power.

pure TiS_3 modes, indicating that the TiS_3 maintains its original crystal structure. However, at 10 mW, additional modes located at 230 cm^{-1} and 330 cm^{-1} appear, indicating that the TiS_3 is partially converted to TiS_2 (black arrows indicated in the figure). The TiS_3 modes no longer exist at the higher power of 15 mW, indicating that the TiS_3 is fully converted to TiS_2.

Figure 3B shows the Raman spectra collected from a 70 nm thick flake at a constant power of 12 mW. The spectra that correspond to pure TiS_3 are observed with increased irradiation times from 10 s to 120 s. However, when the laser power is slightly increased from 12 mW to 13 mW, the co-existence of TiS_3 and TiS_2 appear immediately after a short irradiation time of 10 s (orange curve in Figure 3B). This finding suggests the existence of a clear power threshold although it is thickness dependent. Since it has been reported that the thermal annealing to TiS_3 in a vacuum at high temperatures can convert it to TiS_2,[31,32] while the focused laser irradiation can heat the flakes locally, we deduce that the transformation from TiS_3 to TiS_2 is also a heating-related process. This transformation could be described using the following thermal decomposition mechanism:

$$TiS_3(s) \xrightarrow{laser} TiS_2(s) + S(g)\uparrow \qquad \text{(Equation 1)}$$

where extra sulfur atoms can escape above the TiS_3 decomposition temperature approximately 460°C, which is estimated from the phase diagram of the Ti-S system due to the laser heating effect.[41] The formation of TiS_2 is accompanied with a direct vaporization of sulfur through a sublimation process. The higher temperature converts a larger ratio of TiS_3 to TiS_2, which is consistent with our observation in Figure 3A. Since the conversion occurs within the regions of the moving laser spot, the formation of polycrystalline structures is expected, which is consistent with the increase of surface roughness after irradiation. Meanwhile, compared to the thermal annealing process, laser irradiation can locally modify the lattice at a micrometer scale with through its diffraction-limited focused beam, while the conversion time can be largely reduced at typical annealing temperatures (e.g., 600°C in ref. 32), thus providing a higher flexibility and controllability to the structural transformation from TiS_3 to TiS_2.

Figure 3C shows the Raman spectra obtained from four TiS_3 flakes with different thicknesses (7 nm, 28 nm, 70 nm, and 150 nm) after irradiation with a laser power of 20 mW. The TiS_3 lattice is maintained in the 7 nm thin flake while the 28 nm and 70 nm flakes completely transform to TiS_2. The 150 nm thick flake shows a hybrid composite of TiS_3 and TiS_2. The observed thickness-dependent structural evolution can be understood by considering the heat transport process within the flake. For thin flakes, such as the 7 nm flake in Figure 3C, the absorption is limited and the SiO_2/Si substrate acts as a heat sink, thus preventing the raise of flake temperature to its decomposition temperature. However, for the thick flakes, the heat diffusion will generate a temperature gradient in the c-axis of the crystal. Only layers on the top part can be completely converted to TiS_2 and the bottom layers are maintained as TiS_3. Hence the hybrid structures of TiS_3 and TiS_2 are expected. This explanation is further supported by the use of substrates with different thermal conductivities, which strongly modulate the transformation
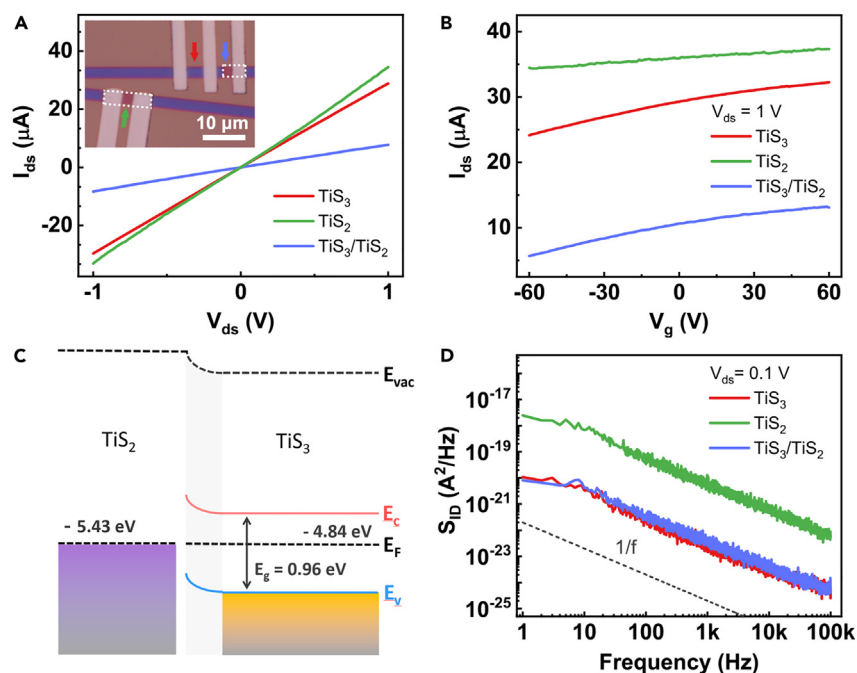
Figure 4. Electrical properties of the pristine TiS₃, the transformed TiS₂, and the TiS₃/TiS₂ junction

(A) I_{ds}-V_{ds} response for the channels of TiS₃, TiS₂, and TiS₃/TiS₂ junction, respectively. The applied back gate voltage bias (V_g) is 0 V. The inset figure is optical image of the devices, channels of which are indicated by the colored arrows; laser converted TiS₂ regions are outlined by white dashed rectangles. The scale bar is 10 μm.

(B) I_{ds}-V_g response of three channels under the constant bias voltage V_{ds} = 1 V.

(C) Band alignment of TiS₂-TiS₂ heterostructure. The calculated values of work function for TiS₂ and TiS₃ are 5.43 eV and 4.84 eV, respectively. The calculated band gap for TiS₃ is 0.96 eV.

(D) Low-frequency noise spectra for the three channels under the bias voltage V_{ds} = 0.1 V and gate voltage V_g = 0 V. The ideal 1/f slope is presented in the figure as a reference.

temperatures. As demonstrated in Figures S2 and S3, the threshold laser power is as low as 4 mW to convert a TiS₃ flake to TiS₂ using a Poly-dimethylsiloxane (PDMS) substrate, whereas no transformation occurs at a power of 20 mW after transferring the TiS₃ flake onto the Si substrate.

By investigating this transformation behavior on more flakes, we have established a diagram that correlate the structural transformation with the layer thickness and the excitation power. As shown in Figure 3E, the TiS₃ lattices on SiO₂/Si substrate are maintained at either thin layers (thickness <10 nm) or low laser powers (typically <10 mW), while pure TiS₂ structures can be obtained with a proper thickness (between 10 and 150 nm) and high laser powers.

The ambient condition is also important for structural conversion. Figure 3D presents the Raman spectra of a 35 nm thick TiS₃ flake in air during the laser irradiation. Instead of forming TiS₃/TiS₂ mixed structures, an additional peak located at 146 cm^{-1} is observed when the laser power is increased from 5 mW to 10 mW (indicated by the additional green arrow). The emerged peak can be correlated with the E_g mode of TiO₂, indicating the oxidization of TiS₃ during irradiation.[42] This observation is consistent with previous reports on the instability of TiS₃ in the atmosphere, where it is converted to TiO₂ during heating treatment.[33] Furthermore, even at the highest available laser power of 20 mW, the TiS₃ is not fully converted to TiO₂ and a combination of Raman peaks from TiS₃, TiS₂, and TiO₂ are present as shown in Figure 3D. Hence, we deduce that the oxidation is a self-limited process that occurs near the surface, preventing further oxidation in the flake and covering the transformed TiS₂ region. This oxidation effect can be minimized by encapsulating TiS₃ with hexagonal-boron nitride (h-BN) layers. The corresponding Raman spectrum (the purple line in Figure 3E) only shows the modes of TiS₂, with no signs of TiS₃ or TiO₂, indicating that the h-BN protected TiS₃ can also be converted to TiS₂.

The different electronic band structures of TiS₃ and TiS₂ show distinct electrical behaviors. Theoretical calculations report that the TiS₃ thin layer is a semiconductor with a band gap of 0.96 eV, while the 1T-TiS₂ tends to be a metal (density of states in Figures S4 in the supplemental information).[21,43] We converted part of the TiS₃ flake with laser-irradiation and formed three different regions, including the pristine TiS₃, converted TiS₂, and the TiS₃/TiS₂ heterojunction as shown in Figure 4A (inset), and then investigated the electrical properties of these regions respectively. Figure 4A presents the current-voltage (I-V_{ds}) relation without the back-gate voltage (V_g) control. All I-V_{ds} curves exhibit linear response, indicating Ohmic contacts between electrodes and the underlying channel materials. Meanwhile, larger resistance is observed in the TiS₃/TiS₂ channel compared with the values in both the TiS₃ and TiS₂ channels. The transconductance defined by $g_m = \frac{\Delta I_{ds}}{\Delta V_g}$ also shows different responses between in these three channels. Figure 4B shows the back-gate voltage response for the three channels under constant
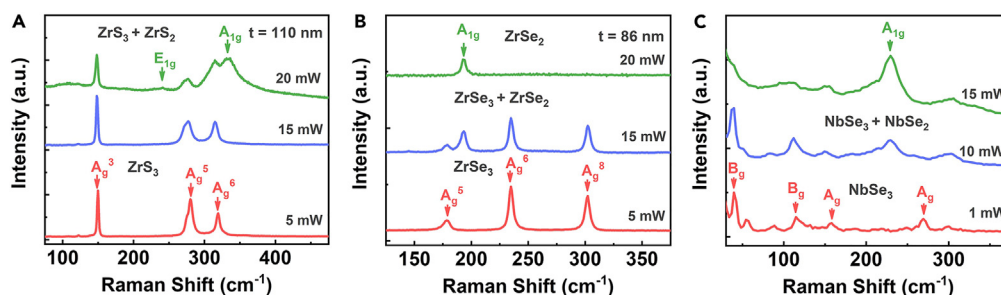
Figure 5. Structural transformation in other MX_3 materials induced by laser-irradiation

(A) Raman spectra of ZrS_3 irradiated with different laser powers in vacuum.

(B) Raman spectra of $ZrSe_3$ irradiated with different laser powers in vacuum.

(C) Raman spectra of $NbSe_3$ irradiated with different laser powers in vacuum.

drain-source voltage bias (V_{ds}) of +1 V. The pristine TiS_3 exhibits the n-type response with a low on-off ratio of ~1.3 in the ± 60 V region of the applied gate voltages. The low on-off ratio may be attributed to its sheet-like geometry with heavy doping, which is reported to exhibit a low on-off ratio with high electrical conductivity.[27] Conversely, the converted TiS_2 exhibits a weaker gate response, corresponding to a higher carrier density with a narrow band gap of TiS_2, which might be attributed to the introduce of sulfur vacancies in the channel during the laser irradiation process. Moreover, the TiS_3/TiS_2 heterojunction shows a similar value of on-off ratio compared with TiS_3 (~2.2) while exhibits much lower drain-source current. Such lower drain-source current in the channel of heterojunction may be attributed to the band structure misalignment between TiS_3 and TiS_2, as shown in Figure 4C. Metallic TiS_2 is calculated to have a larger work function (calculated to be ~5.43 eV) than semiconducting TiS_3 (~4.84 eV), which is approximately 0.59 eV. Although this value may be reduced by additional doping in two materials that raise their Fermi levels, an additional potential barrier can still be established that reduces the junction current. Figure 4D shows the low-frequency noise spectra for these three regions. All of these spectra exhibit a typical 1/f slope (dashed line in the figure).[44] The original TiS_3 and its heterojunction with TiS_2 have the same level of noise density despite their different drain-source current, while the value for the converted TiS_2 is approximately two orders larger. Such difference might be attributed to the larger fluctuations of carrier numbers and the correlated mobility caused by the inducing of additional defects during laser irradiation. Although TiS_3 has been reported to have ultra-high photoresponse,[28] all the three channels in our device show ignorable photoresponse (Figures S5 in the supplemental information). We also attribute it to the sheet-like geometry, which results poor photoresponse compared with TiS_3 nanoribbons.[27]

Besides TiS_3, we discover that this laser irradiation induced structure transformation can occur in other MX_3 materials. Figure 5A shows the Raman spectra of a 110 nm thick ZrS_3 flake irradiated with different laser powers. At the highest power of 20 mW, additional Raman peaks corresponding to the E_{1g} and A_{1g} modes of ZrS_2 shows up in addition to Raman modes of ZrS_3, indicating a composition of ZrS_3 and ZrS_2. We also find the laser irradiation can completely covert an 86 nm thick $ZrSe_3$ flake to $ZrSe_2$ as shown in Figure 5B. Interestingly, this transformation is not limited in the group IV MX_3 materials, as shown in Figure 5C, which displays the Raman spectra of $NbSe_3$ under laser irradiation. The relatively low power of 10 mW can induce the hybrid structures of $NbSe_3$ and $NbSe_2$. This transformation process can be explained by the relatively lower crystallization temperatures of MX_3 compared to the corresponding MX_2 materials. Meanwhile, laser irradiations on transition-metal-tellurides, such as $ZrTe_3$ and $ZrTe_5$, form tellurium nanostructures instead of transition metal ditellurides (e.g., $ZrTe_2$). Such results are also widely observed in other transition-metal-tellurides,[45] possible due to the thermal instability of tellurides with higher sublimation temperatures of tellurium (Figure S6 in the supplemental information). Thus, the laser irradiation method provides a way to modulate the structures and properties of transition-metal-trichalcogenides with high controllability and spatial resolution.

Conclusions

In conclusion, we have systematically studied the structural transformation from the layered TiS_3 to TiS_2 induced by laser irradiations. A transformation diagram is established by investigating the relation between converted products and varied laser powers and flake thickness. The underlying mechanism is attributed to the pyrolysis of TiS_3 caused by the irradiation-induced heating effect. The transformation can induce a change of the electrical transport properties and surface potential in the original van der Waals materials by controlling the amount of the converted TiS_2 flakes. Moreover, such structural transformation occurs in many other trichalcogenide materials. Our work demonstrates the controllability of inducing structural transformations in trichalcogenides using laser irradiation, thus broadening their applications to low-dimensional electronic and optoelectronic devices in the future.

STAR★METHODS

Detailed methods are provided in the online version of this paper and include the following:

- KEY RESOURCES TABLE
- RESOURCE AVAILABILITY
  - Lead contact

SUPPLEMENTAL INFORMATION

Supplemental information can be found online at https://doi.org/10.1016/j.isci.2023.107895.

AUTHOR CONTRIBUTIONS

Y.Z. and Y.Q.B. supervised the project. H.Z. and X.T. fabricated the samples, conducted the laser irradiation and the related measurements. Z.W. and S.W. conducted AFM measurements and analyzed the results. J.G. synthesized the crystals. L.F. conducted EDS measurements. X.L. and J.Y. did the DFT simulations. Y.Z., Y.Q.B., H.Z., and X.T. wrote the paper. All authors analyzed the results and approved the current version of the article. H.Z. and X.T. contributed equally to this work.

DECLARATION OF INTERESTS

The authors declare no competing interests.

REFERENCES

1. Kollipara, P.S., Li, J., and Zheng, Y. (2020). Optical Patterning of Two-Dimensional Materials. Research *2020*, 6581250. https://doi.org/10.34133/2020/6581250.

2. Li, Z., and Chen, F. (2017). Ion beam modification of two-dimensional materials: Characterization, properties, and applications. Appl. Phys. Rev. *4*, 011103. https://doi.org/10.1063/1.4977087.

3. Fox, D.S., Zhou, Y., Maguire, P., O'Neill, A., Ó'Coileáin, C., Gatensby, R., Glushenkov, A.M., Tao, T., Duesberg, G.S., Shvets, I.V., et al. (2015). Nanopatterning and Electrical Tuning of MoS$_2$ Layers with a Subnanometer Helium Ion Beam. Nano Lett. *15*, 5307–5313. https://doi.org/10.1021/acs.nanolett.5b01673.

4. Zhou, Y., Jadwiszczak, J., Keane, D., Chen, Y., Yu, D., and Zhang, H. (2017). Programmable graphene doping via electron beam irradiation. Nanoscale *9*, 8657–8664. https://doi.org/10.1039/C7NR03446F.

5. Kim, T.-Y., Cho, K., Park, W., Park, J., Song, Y., Hong, S., Hong, W.-K., and Lee, T. (2014). Irradiation Effects of High-Energy Proton Beams on MoS$_2$ Field Effect Transistors. ACS Nano *8*, 2774–2781. https://doi.org/10.1021/nn4064924.

6. Castellanos-Gomez, A., Barkelid, M., Goossens, A.M., Calado, V.E., van der Zant, H.S.J., and Steele, G.A. (2012). Laser-Thinning of MoS$_2$: On Demand Generation of a Single-Layer Semiconductor. Nano Lett. *12*, 3187–3192. https://doi.org/10.1021/nl301164v.

7. Hu, L., Shan, X., Wu, Y., Zhao, J., and Lu, X. (2017). Laser Thinning and Patterning of MoS$_2$ with Layer-by-Layer Precision. Sci. Rep. *7*, 15538. https://doi.org/10.1038/s41598-017-15350-4.

8. Lu, J., Wu, J., Carvalho, A., Ziletti, A., Liu, H., Tan, J., Chen, Y., Castro Neto, A.H., Özyilmaz, B., and Sow, C.H. (2015). Bandgap Engineering of Phosphorene by Laser Oxidation toward Functional 2D Materials. ACS Nano *9*, 10411–10421. https://doi.org/10.1021/acsnano.5b04623.

9. Wang, B., Peng, R., Wang, X., Yang, Y., Wang, E., Xin, Z., Sun, Y., Li, C., Wu, Y., Wei, J., et al. (2021). Ultrafast, Kinetically Limited, Ambient Synthesis of Vanadium Dioxides through Laser Direct Writing on Ultrathin Chalcogenide Matrix. ACS Nano *15*, 10502–10513. https://doi.org/10.1021/acsnano.1c03050.

10. Cho, S., Kim, S., Kim, J.H., Zhao, J., Seok, J., Keum, D.H., Baik, J., Choe, D.-H., Chang, K.J., Suenaga, K., et al. (2015). Phase patterning for ohmic homojunction contact in MoTe$_2$. Science *349*, 625–628. https://doi.org/10.1126/science.aab3175.

11. Mine, H., Kobayashi, A., Nakamura, T., Inoue, T., Pakdel, S., Marian, D., Gonzalez-Marin, E., Maruyama, S., Katsumoto, S., Fortunelli, A., et al. (2019). Laser-Beam-Patterned Topological Insulating States on Thin Semiconducting MoS$_2$. Phys. Rev. Lett. *123*, 146803. https://doi.org/10.1103/PhysRevLett.123.146803.

12. Zhang, J., Han, J., Peng, G., Yang, X., Yuan, X., Li, Y., Chen, J., Xu, W., Liu, K., Zhu, Z., et al. (2020). Light-induced irreversible structural phase transition in trilayer graphene. Light Sci. Appl. *9*, 174. https://doi.org/10.1038/s41377-020-00412-6.

13. Randle, M., Lipatov, A., Kumar, A., Kwan, C.-P., Nathawat, J., Barut, B., Yin, S., He, K., Arabchigavkani, N., Dixit, R., et al. (2019). Gate-Controlled Metal–Insulator Transition in TiS$_3$ Nanowire Field-Effect Transistors. ACS Nano *13*, 803–811. https://doi.org/10.1021/acsnano.8b08260.

14. Huang, C., Zhang, E., Yuan, X., Wang, W., Liu, Y., Zhang, C., Ling, J., Liu, S., and Xiu, F.

(2017). Tunable charge density wave in TiS$_3$ nanoribbons. Chinese Phys. B 26, 067302. https://doi.org/10.1088/1674-1056/26/6/067302.

15. Papadopoulos, N., Flores, E., Watanabe, K., Taniguchi, T., Ares, J.R., Sanchez, C., Ferrer, I.J., Castellanos-Gomez, A., Steele, G.A., and van der Zant, H.S.J. (2019). Multi-terminal electronic transport in boron nitride encapsulated TiS$_3$ nanosheets. 2D Mater. 7, 015009. https://doi.org/10.1088/2053-1583/ab4ef3.

16. Khatibi, A., Godiksen, R.H., Basuvalingam, S.B., Pellegrino, D., Bol, A.A., Shokri, B., and Curto, A.G. (2019). Anisotropic infrared light emission from quasi-1D layered TiS$_3$. 2D Mater. 7, 015022. https://doi.org/10.1088/2053-1583/ab57ef.

17. Kong, W., Bacaksiz, C., Chen, B., Wu, K., Blei, M., Fan, X., Shen, Y., Sahin, H., Wright, D., Narang, D.S., and Tongay, S. (2017). Angle resolved vibrational properties of anisotropic transition metal trichalcogenide nanosheets. Nanoscale 9, 4175–4182. https://doi.org/10.1039/C7NR00711F.

18. Papadopoulos, N., Frisenda, R., Biele, R., Flores, E., Ares, J.R., Sánchez, C., van der Zant, H.S.J., Ferrer, I.J., D'Agosta, R., and Castellanos-Gomez, A. (2018). Large birefringence and linear dichroism in TiS$_3$ nanosheets. Nanoscale 10, 12424–12429. https://doi.org/10.1039/C8NR03616K.

19. Hou, S., Guo, Z., Yang, J., Liu, Y.-Y., Shen, W., Hu, C., Liu, S., Gu, H., and Wei, Z. (2021). Birefringence and Dichroism in Quasi-1D Transition Metal Trichalcogenides: Direct Experimental Investigation. Small 17, 2100457. https://doi.org/10.1002/smll.202100457.

20. Molina-Mendoza, A.J., Barawi, M., Biele, R., Flores, E., Ares, J.R., Sánchez, C., Rubio-Bollinger, G., Agraït, N., D'Agosta, R., Ferrer, I.J., and Castellanos-Gomez, A. (2015). Electronic Bandgap and Exciton Binding Energy of Layered Semiconductor TiS$_3$. Adv. Electron. Mater. 1, 1500126. https://doi.org/10.1002/aelm.201500126.

21. Jin, Y., Li, X., and Yang, J. (2015). Single layer of MX$_3$ (M = Ti, Zr; X = S, Se, Te): a new platform for nano-electronics and optics. Phys. Chem. Chem. Phys. 17, 18665–18669. https://doi.org/10.1039/C5CP02813B.

22. Dai, J., and Zeng, X.C. (2015). Titanium Trisulfide Monolayer: Theoretical Prediction of a New Direct-Gap Semiconductor with High and Anisotropic Carrier Mobility. Angew. Chem. 127, 7682–7686. https://doi.org/10.1002/ange.201502107.

23. Island, J.O., Molina-Mendoza, A.J., Barawi, M., Biele, R., Flores, E., Clamagirand, J.M., Ares, J.R., Sánchez, C., van der Zant, H.S.J., D'Agosta, R., et al. (2017). Electronics and optoelectronics of quasi-1D layered transition metal trichalcogenides. 2D Mater. 4, 022003. https://doi.org/10.1088/2053-1583/aa6ca6.

24. Tripathi, N., Pavelyev, V., Sharma, P., Kumar, S., Rymzhina, A., and Mishra, P. (2021). Review of titanium trisulfide (TiS$_3$): A novel material for next generation electronic and optical devices. Mater. Sci. Semicond. Process. 127, 105699. https://doi.org/10.1016/j.mssp.2021.105699.

25. Niu, Y., Frisenda, R., Flores, E., Ares, J.R., Jiao, W., Perez de Lara, D., Sánchez, C., Wang, R., Ferrer, I.J., and Castellanos-Gomez, A. (2018). Polarization-Sensitive and Broadband Photodetection Based on a Mixed-Dimensionality TiS$_3$/Si p–n Junction. Adv. Opt. Mater. 6, 1800351. https://doi.org/10.1002/adom.201800351.

26. Liu, S., Xiao, W., Zhong, M., Pan, L., Wang, X., Deng, H.-X., Liu, J., Li, J., and Wei, Z. (2018). Highly polarization sensitive photodetectors based on quasi-1D titanium trisulfide (TiS$_3$). Nanotechnology 29, 184002. https://doi.org/10.1088/1361-6528/aaafa2.

27. Island, J.O., Barawi, M., Biele, R., Almazán, A., Clamagirand, J.M., Ares, J.R., Sánchez, C., van der Zant, H.S.J., Álvarez, J.V., D'Agosta, R., et al. (2015). TiS$_3$ Transistors with Tailored Morphology and Electrical Properties. Adv. Mater. 27, 2595–2601. https://doi.org/10.1002/adma.201405632.

28. Island, J.O., Buscema, M., Barawi, M., Clamagirand, J.M., Ares, J.R., Sánchez, C., Ferrer, I.J., Steele, G.A., van der Zant, H.S.J., and Castellanos-Gomez, A. (2014). Ultrahigh Photoresponse of Few-Layer TiS$_3$ Nanoribbon Transistors. Adv. Opt. Mater. 2, 641–645. https://doi.org/10.1002/adom.201400043.

29. Baraghani, S., Abourahma, J., Barani, Z., Mohammadzadeh, A., Sudhindra, S., Lipatov, A., Sinitskii, A., Kargar, F., and Balandin, A.A. (2021). Printed Electronic Devices with Inks of TiS3 Quasi-One-Dimensional van der Waals Material. ACS Appl. Mater. Interfaces 13, 47033–47042. https://doi.org/10.1021/acsami.1c12948.

30. Lv, X., Huang, X., Zhang, W., Deng, C., Chen, F., Wang, Y., Long, J., Gao, H., Deng, L., Ye, L., and Xiong, W. (2022). High-Responsivity Multiband and Polarization-Sensitive Photodetector Based on the TiS$_3$/MoS$_2$ Heterojunction. ACS Appl. Mater. Interfaces 14, 48812–48820. https://doi.org/10.1021/acsami.2c12332.

31. Nath, M., and Rao, C.N.R. (2002). Nanotubes of Group 4 Metal Disulfides. Angew. Chem. Int. Ed. 41, 3451–3454. https://doi.org/10.1002/1521-3773(20020916)41:18<3451::AID-ANIE3451>3.0.CO;2-2.

32. Wu, X.C., Tao, Y.R., and Gao, Q.X. (2009). Preparation and field emission properties of titanium polysulfide nanobelt films. Nano Res. 2, 558–564. https://doi.org/10.1007/s12274-009-9055-2.

33. Ghasemi, F., Frisenda, R., Flores, E., Papadopoulos, N., Biele, R., Perez de Lara, D., van der Zant, H.S.J., Watanabe, K., Taniguchi, T., D'Agosta, R., et al. (2020). Tunable Photodetectors via In Situ Thermal Conversion of TiS$_3$ to TiO$_2$. Nanomaterials 10, 711. https://doi.org/10.3390/nano10040711.

34. Guo, Y., Tao, J., Zhang, Z., Fei, L., Li, D., Jadwiszczak, J., Wang, X., Guo, Y., Liao, X., and Zhou, Y. (2020). Controllable Thermal Oxidation and Photoluminescence Enhancement in Quasi-1D van der Waals ZrS$_3$ Flakes. ACS Appl. Electron. Mater. 2, 3756–3764. https://doi.org/10.1021/acsaelm.0c00788.

35. Osada, K., Bae, S., Tanaka, M., Raebiger, H., Shudo, K., and Suzuki, T. (2016). Phonon Properties of Few-Layer Crystals of Quasi-One-Dimensional ZrS$_3$ and ZrSe$_3$. J. Phys. Chem. C 120, 4653–4659. https://doi.org/10.1021/acs.jpcc.5b12441.

36. Pant, A., Torun, E., Chen, B., Bhat, S., Fan, X., Wu, K., Wright, D.P., Peeters, F.M., Soignard, E., Sahin, H., and Tongay, S. (2016). Strong dichroic emission in the pseudo one dimensional material ZrS$_3$. Nanoscale 8, 16259–16265. https://doi.org/10.1039/C6NR05238J.

37. Lipatov, A., Loes, M.J., Lu, H., Dai, J., Patoka, P., Vorobeva, N.S., Muratov, D.S., Ulrich, G., Kästner, B., Hoehl, A., et al. (2018). Quasi-1D TiS$_3$ Nanoribbons: Mechanical Exfoliation and Thickness-Dependent Raman Spectroscopy. ACS Nano 12, 12713–12720. https://doi.org/10.1021/acsnano.8b07703.

38. Pawbake, A.S., Island, J.O., Flores, E., Ares, J.R., Sanchez, C., Ferrer, I.J., Jadkar, S.R., van der Zant, H.S.J., Castellanos-Gomez, A., and Late, D.J. (2015). Temperature-Dependent Raman Spectroscopy of Titanium Trisulfide (TiS$_3$) Nanoribbons and Nanosheets. ACS Appl. Mater. Interfaces 7, 24185–24190. https://doi.org/10.1021/acsami.5b07492.

39. Tanaka, R., Yuge, K., Kawai, J., and Alawadhi, H. (2017). Artificial peaks in energy dispersive X-ray spectra: sum peaks, escape peaks, and diffraction peaks. X Ray Spectrom. 46, 5–11. https://doi.org/10.1002/xrs.2697.

40. Hawkins, C.G., and Whittaker-Brooks, L. (2018). Controlling Sulfur Vacancies in TiS$_{2-x}$ Cathode Insertion Hosts via the Conversion of TiS3 Nanobelts for Energy-Storage Applications. ACS Appl. Nano Mater. 1, 851–859. https://doi.org/10.1021/acsanm.7b00266.

41. Mikkelsen, J.C. (2007). P-T-X phase diagram for Ti—S from (60÷75) atomic % sulfur. Nuov. Cim. B 38, 378–386. https://doi.org/10.1007/BF02723508.

42. Ohsaka, T., Izumi, F., and Fujiki, Y. (1978). Raman spectrum of anatase, TiO$_2$. J. Raman Spectrosc. 7, 321–324. https://doi.org/10.1002/jrs.1250070606.

43. Wang, H., Qiu, Z., Xia, W., Ming, C., Han, Y., Cao, L., Lu, J., Zhang, P., Zhang, S., Xu, H., and Sun, Y.-Y. (2019). Semimetal or Semiconductor: The Nature of High Intrinsic Electrical Conductivity in TiS$_2$. J. Phys. Chem. Lett. 10, 6996–7001. https://doi.org/10.1021/acs.jpclett.9b02710.

44. Balandin, A.A. (2013). Low-frequency 1/f noise in graphene devices. Nat Nano 8, 549–555. https://doi.org/10.1038/nnano.2013.144.

45. Manjón, F.J., Gallego-Parra, S., Rodríguez-Hernández, P., Muñoz, A., Drasar, C., Muñoz-Sanjosé, V., and Oeckler, O. (2021). Anomalous Raman modes in tellurides. J. Mater. Chem. C 9, 6277–6289. https://doi.org/10.1039/D1TC00980J.

46. Island, J.O., Biele, R., Barawi, M., Clamagirand, J.M., Ares, J.R., Sánchez, C., van der Zant, H.S.J., Ferrer, I.J., D'Agosta, R., and Castellanos-Gomez, A. (2016). Titanium trisulfide (TiS$_3$): a 2D semiconductor with quasi-1D optical and electronic properties. Sci. Rep. 6, 22214. https://doi.org/10.1038/srep22214.

47. Castellanos-Gomez, A., Buscema, M., Molenaar, R., Singh, V., Janssen, L., van der Zant, H.S.J., and Steele, G.A. (2014). Deterministic Transfer of Two-dimensional Materials by All-dry Viscoelastic Stamping. 2D Mater. 1, 011002. https://doi.org/10.1088/2053-1583/1/011002.

48. Kresse, G., and Furthmüller, J. (1996). Efficiency of ab-initio total energy calculations for metals and

semiconductors using a plane-wave basis set. Comput. Mater. Sci. *6*, 15–50. https://doi.org/10.1016/0927-0256(96)00008-0.

49. Kresse, G., and Furthmüller, J. (1996). Efficient iterative schemes for ab initio total-energy calculations using a plane-wave basis set.

Phys. Rev. B *54*, 11169–11186. https://doi.org/10.1103/PhysRevB.54.11169.

50. Perdew, J.P., Burke, K., and Ernzerhof, M. (1996). Generalized Gradient Approximation Made Simple. Phys. Rev. Lett. *77*, 3865–3868. https://doi.org/10.1103/PhysRevLett.77.3865.

51. Dudarev, S.L., Botton, G.A., Savrasov, S.Y., Humphreys, C.J., and Sutton, A.P. (1998). Electron-energy-loss spectra and the structural stability of nickel oxide: An LSDA+U study. Phys. Rev. B *57*, 1505–1509. https://doi.org/10.1103/PhysRevB.57.1505.

STAR★METHODS

KEY RESOURCES TABLE

REAGENT or RESOURCE	SOURCE	IDENTIFIER
Other		
Silicon Wafer (285 nm SiO 2/Si)	Yilan Microelectronics	http://www.yilanmicro.com/

RESOURCE AVAILABILITY

Lead contact

Further information and requests for resources and reagents should be directed to and will be fulfilled by the Lead Contact, Ya-Qing Bie (bieyq@mail.sysu.edu.cn) and Yangbo Zhou (yangbozhou@ncu.edu.cn).

Materials availability

All materials used and generated in this study will be made available on request from the lead contact with a completed Materials Transfer Agreement.

Data and code availability

- Raman, AFM and electrical measurements data reported in this paper will be shared by the lead contact upon request.
- This paper does not report original codes.
- Any additional information required to reanalyze the data reported in this paper is available from the lead contact upon request.

EXPERIMENTAL MODEL AND SUBJECT DETAILS

Sample preparation

High-quality TiS_3 bulk crystals were synthesized using the conventional chemical vapor transport process.[46] High purity Titanium (99.999%) and sulfur (99.9%) powders were mixed at a stoichiometric ratio of 1:3 and sealed in a quartz tube at high vacuum ($<10^{-4}$ Torr). The tube was placed in a two-zone furnace with the hot zone maintained at 550° C and the cold zone maintained at 450°C for seven days. Then the tube was cooled naturally to room temperature to obtain needle-like crystals. Other crystals used in the experiments (e.g., TiS_2, ZrS_3, and others) are either synthesized using the same method. The thin flakes were mechanically exfoliated and transferred onto SiO_2/Si substrates using a PDMS-assisted stamp transfer method.[47]

METHOD DETAILS

Optical characterizations and laser irradiations

An optical microscope (Nikon Ci-Pol) was used to identify the geometry and location of the transferred TiS_3 flakes on substrates. Their thickness was confirmed by AFM measurements. The Raman spectra were obtained using a commercial confocal Raman Microscope (Witec Alpha 300R). This system provides a 532 nm laser with diffraction-limited beam spot (<400 nm), and the delivered laser power can be precisely adjusted from 0.1 mW to 20 mW with 0.1 mW precision. The laser irradiation experiments were carried out on the same system, and the samples were placed in the vacuum chamber of an optical cryostat (CIA C04-002-007, pressure $<10^{-2}$ Pa). The laser beam was focused on the flake using a glass thickness corrected objective lens (50 ×, N.A. = 0.7, spot size ~460 nm). A different objective lens (100 ×, N.A. = 0.9, spot size ~360 nm) was used for the laser scanning process in air as shown in Figure 3D.

AFM characterizations

The tapping mode in an AFM (Asylum Cipher ES) was applied to obtain the thickness information of the selected flakes. The kelvin probe force microscopy (KPFM) mode in the same instruments was also applied to investigate the surface potential variations after laser irradiations.

Device fabrication and electrical characterizations

TiS_3 field-effect transistors with multiple electrical contacts were fabricated through the traditional microfabrication process. These contacts were first patterned by a standard electron beam lithography (EBL) process, followed by the deposition of a metal film (10 nm Ti and 50 nm Ni) with a lift-off process. The electrical characterizations to the fabricated devices were carried out by placing them in a vacuum probe station (Lakeshore CRX VF, vacuum pressure $< 5 \times 10^{-1}$ mbar). All the electrical measurements were carried out using a semiconductor parameter analyzer (PDA FS-Pro) at room temperature without light illumination.

The EDS analysis

The EDS spectra from thin TiS3 flakes were collected using an energy-dispersive X-ray spectrometer (Oxford Instruments, UltimMax 65), which is installed on a Thermoscientific Scios2 dual beam scanning electron microscope. A 20 kV electron beam with current of 0.8 nA were used to collect the spectra.

Theoretical calculations

All the first-principles calculations were performed by density functional theory (DFT) based Vienna *ab initio* Simulation Package (VASP).[48] A plane-wave basis set with a cutoff energy of 450 eV was employed.[49] Perdew-Burke-Ernzerhof (PBE) within the generalized gradient approximation (GGA) is chosen for the exchange-correlation functional.[50] The DFT+U method is carried out to deal with electron correlations for transition metal Ti atom with U_{eff} = 5.8 eV.[51] The TiS_3 and TiS_2 were simulated by slab model with a 15 Å vacuum layer. The density of states and average electrostatic potential were computed using a 13 × 13×1 *k*-point mesh for the slab geometries. The convergence criterion was set to be 10^{-5} eV. The structures are fully relaxed until the force for all atoms is less than 10^{-3} eV/Å.